

# Toward triggered generation of indistinguishable single-photons from MoTe<sub>2</sub> quantum emitters

Paweł Wyborski,<sup>1</sup> Athanasios Paralakis,<sup>1</sup> Pietro Metuh,<sup>1</sup> Martin A. Jacobsen,<sup>1</sup> Christian Ruiz,<sup>1</sup> Niels Gregersen,<sup>1</sup> and Battulga Munkhbat<sup>1,\*</sup>

<sup>1</sup>*Department of Electrical and Photonics Engineering, Technical University of Denmark, 2800 Kgs. Lyngby, Denmark*

Single-photon sources operating in the telecom band are fundamental components for long-distance optical quantum communication and information processing. Two-dimensional (2D) transition metal dichalcogenides (TMDs) offer a promising platform for such sources, but their development has been hindered by limited spectral range and poor single-photon indistinguishability. Here, we demonstrate a reproducible and systematic approach for generating near-infrared (1090–1200 nm) quantum emitters in bilayer MoTe<sub>2</sub> using deterministic strain and defect engineering. These emitters exhibit strong linear polarization (DOLP > 70%), sub-nanosecond lifetimes ( $\tau \leq 450$  ps), high single-photon purity ( $g^{(2)}(0) < 0.1$ ), and resolution-limited emission ( $\sim 200$   $\mu$ eV). Electrostatic biasing enables Stark tuning over a  $\sim 3$  meV range, reduced photon bunching, and significantly shortened radiative lifetimes, yielding narrow emission with ratios of experimental to transform-limited linewidths as low as  $R \sim 55$ . Most notably, two-photon interference measurements reveal a Hong-Ou-Mandel visibility of  $V_{\text{HOM}} \sim 10\%$ , and up to  $V_{\text{HOM}} \sim 40\%$  with post-selection by temporal filtering, representing the highest reported indistinguishability for any TMD quantum emitters and the first such demonstration in the near-infrared regime. These results establish MoTe<sub>2</sub> as a viable platform for tunable, low-noise, high-purity single-photon sources with promising indistinguishability, paving the way for their integration into telecom-compatible quantum photonic technologies.

Keywords: Quantum emitters, single-photon emission, MoTe<sub>2</sub>, TMDs, hBN encapsulation, Stark shift, Indistinguishability

## I. INTRODUCTION

The generation of on-demand, indistinguishable single photons is essential for advancing photonic quantum technologies, enabling quantum interference, entanglement distribution, and scalable quantum computing architectures [1, 2]. Operating at longer wavelengths, particularly within the telecom band, is highly advantageous as it leverages existing low-loss optical fiber infrastructure and ensures compatibility with classical communication networks, thereby enabling long-distance quantum communication with minimal transmission loss [3, 4].

Two-dimensional (2D) transition metal dichalcogenides (TMDs) have emerged as a promising platform for quantum photonics [5], offering efficient photon extraction due to their atomically thin geometries [6], along with tunable emission and strong light-matter interactions [7–10]. Their innate ability to form van der Waals heterostructures enables the engineering of novel optical properties and facilitates integration with existing photonic platforms [11–13]. Among their many advantages, 2D TMDs can host localized quantum emitters (QEs) that operate as single-photon sources, with emission energies tunable through strain, defect engineering, and electrostatic control [14–24]. Localized quantum emitters (QEs) in TMDs are typically created by coupling local strain fields with defect sites [21, 23–25], giving rise to confined excitonic states that exhibit quantum light emission. These emitters have been demonstrated across

various TMD materials and spectral ranges [13], with most reports focused on tungsten-based compounds such as WSe<sub>2</sub> operating in the visible regime [13–18, 21, 26–34]. While these systems can achieve high single-photon purity [17, 21, 33, 35–38] and spectral tunability [20, 39–41], their limited indistinguishability of only  $\sim 2\%$  [33] and short emission wavelengths constrain their use in long-distance quantum networks.

Molybdenum-based TMDs such as MoTe<sub>2</sub> offer emission in the near-infrared (NIR), overlapping with telecom-relevant windows. However, quantum emitters in MoTe<sub>2</sub> have remained largely unexplored, with previous demonstrations showing long radiative lifetimes ranging from  $\sim 20$  ns to  $\sim$ ms, broad linewidths exceeding 600  $\mu$ eV, and a lack of reproducibility or tuning [42]. Moreover, no two-photon interference measurements have yet been reported for any MoTe<sub>2</sub>-based emitter, and indistinguishability remains unverified for the entire TMD platform at telecom wavelengths.

In this work, we demonstrate a reproducible and deterministic approach to realizing high-quality and tunable quantum emitters in bilayer MoTe<sub>2</sub>, exhibiting high single-photon purity and promising photon indistinguishability. By combining directional strain engineering with electron-beam-induced defect activation, we generate stable and spectrally narrow emitters across multiple samples, operating in the 1090–1200 nm spectral range. These quantum emitters exhibit fast radiative decays of 130–440 ps, strong linear polarization with degrees of linear polarization (DOLP) up to  $\sim 70\%$ , high single-photon purity ( $g^{(2)}(0) < 0.1$ ), and resolution-limited emission linewidths of  $\sim 200$   $\mu$ eV. Quasi-resonant excitation sup-

\* bamunk@dtu.dk

presses spectral diffusion and enhances purity through background emission reduction, while electrostatic biasing enables active Stark tuning over a  $\sim 3$  meV range, reduces photon bunching, and improves emission stability. A direct comparison of experimental emission linewidths ( $W_{\text{exp}}$ ) and transform-limited linewidths ( $W_{\text{rad}}$ ) reveals ultra-low ratios  $R = W_{\text{exp}}/W_{\text{rad}}$  down to  $R \sim 55$ , indicating significant suppression of charge noise and environmental fluctuations. Most notably, we observe two-photon interference with a Hong–Ou–Mandel visibility of  $V_{\text{HOM}} \sim 10\%$ , and up to  $V_{\text{HOM}} \sim 40\%$  with post-selection (temporal filtering), representing the first demonstration of photon indistinguishability from a TMD-based quantum emitter in the near-infrared. These results establish MoTe<sub>2</sub> and TMD quantum emitters in general as a viable platform for tunable, low-noise single-photon sources capable of generating indistinguishable photons for photonic quantum technologies at telecom wavelengths.

## II. SYSTEM UNDER STUDY

To realize MoTe<sub>2</sub> quantum emitters (QEs), we begin by designing a highly reflective substrate consisting of a bottom distributed Bragg reflector (DBR) made of 20 pairs of GaAs (85.0 nm) and AlAs (99.7 nm) layers grown on a GaAs wafer, capped with an additional 110 nm thick Al<sub>2</sub>O<sub>3</sub> layer (Fig. 1a). This substrate is specifically designed to maximize photon extraction efficiency [6, 33, 43] from MoTe<sub>2</sub> emitters fabricated on top (Fig. 1b), as supported by our optical simulations (see Methods and Supporting Notes S1 and S2 for details on substrate preparation and extraction efficiency calculations). The measured reflectivity of the fabricated DBR substrate (orange line in Fig. 1b) exhibits high reflection (approaching unity) across a broad spectral range from 1100 nm to 1240 nm, well aligned with the emission spectrum of bilayer MoTe<sub>2</sub>. Gold electrodes (5 nm Ti / 50 nm Au) are then fabricated via standard UV photolithography followed by metal deposition and lift-off. To implement directional strain engineering, star-shaped nanopillars are fabricated using a high-resolution negative resist (hydrogen silsesquioxane, or HSQ) via e-beam lithography. The resulting nanopillars are around 150 nm in height and feature a three-pointed star geometry, adapted from our previous work [41]. Bilayer MoTe<sub>2</sub> flakes are mechanically exfoliated from bulk crystals (HQ-Graphene) using the standard scotch-tape method onto a polydimethylsiloxane (PDMS) stamp. The flakes are identified prior to transfer based on their photoluminescence (PL) spectra at room temperature (see Supporting Note S1 and Methods for details). Following identification, the selected bilayers are dry-transferred onto the substrate with pre-patterned nanopillars and electrodes (Fig. 1a). During transfer, the bilayer conforms to the underlying three-pointed star nanopillars, forming nanowrinkles. These strain-induced wrinkle regions act as localized hosts for polarized quantum emitters via directional strain confine-

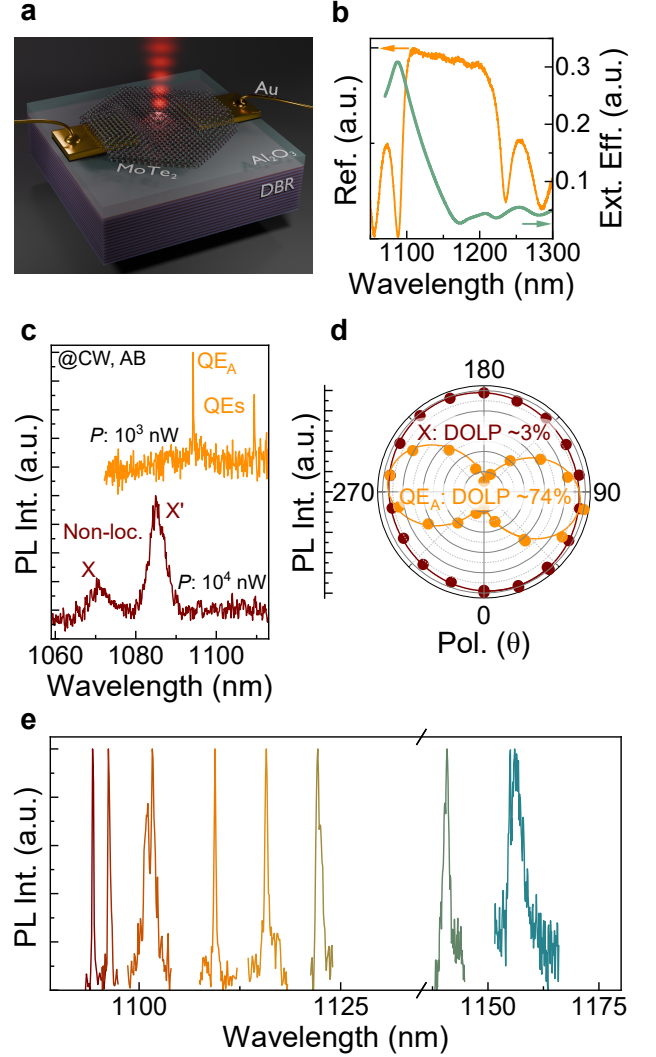


**FIG. 1. Optical characterization of the sample ( $T = 4$  K).** **a)** Schematic of the device architecture. A MoTe<sub>2</sub> bilayer transferred onto a DBR/Al<sub>2</sub>O<sub>3</sub> substrate. Local strain induces a quantum emitter that produces single photons. Gold electrodes contact the flake, enabling electric bias. **b)** Optical characterization of the DBR. The orange curve (left axis) shows near-unity reflectivity between 1100–1240 nm. The green curve (right axis) shows the calculated extraction efficiency, peaking around 1100 nm, well-matched to the MoTe<sub>2</sub> emission range. **c)**  $\mu$ PL spectra under CW 650 nm (AB) excitation. Emission from a strained wrinkle region (orange) shows two sharp peaks (QE<sub>A</sub> and QE<sub>S</sub>) attributed to localized quantum emitters. The unstrained region (dark red) displays broader emission assigned to the non-localized excitonic transition. **d)** Polarization profiles of QE<sub>A</sub> and delocalized excitonic transition X  $\mu$ PL intensity. QE<sub>A</sub> shows strong linear polarization (DOLP  $\sim 74\%$ ), whereas X is unpolarized (DOLP  $\sim 3\%$ ). **e)** Representative emission lines from multiple emitters across the sample.

ment, as demonstrated previously [34]. After the transfer, the strain-localized regions are selectively irradiated

by a focused electron beam to introduce atomic-scale defects, which activate the formation of localized quantum emitters [21, 25, 34].

For initial optical characterization, we performed micro-photoluminescence ( $\mu$ PL) measurements by placing the fabricated sample in a closed-cycle cryostat (attocube attoDRY800XS) operating at  $T \sim 3.9$  K, equipped with a low-temperature objective (NA = 0.80) (further details in Methods). Under above-band (AB) excitation with a 650 nm laser (PicoQuant LDH-D-C-650), narrow PL emission lines were obtained in strained wrinkle regions (orange line, Fig. 1c), consistent with localized states associated with single-photon emission in other TMD-based platforms [21, 25, 34]. In contrast, broader emissions (dark red line) are observed from the unstrained areas, attributed to delocalized exciton recombination [44, 45]. We further investigate the polarization properties of both the narrow emission lines and the broader excitonic peaks. Prior studies have shown that quantum emitters localized in nanowrinkles often exhibit a high degree of linear polarization (DOLP), typically aligned with the wrinkle direction [34]. Consistent with these findings,  $QE_A$  exhibits a pronounced polarization anisotropy, with a DOLP exceeding 70% (Fig. 1d, orange line), in clear contrast to the unpolarized emission from the delocalized excitonic transitions (dark red line). Full characterization of delocalized excitonic transitions and other similar peaks is provided in Supporting Note S3. Lastly, we identified a range of narrow emission lines from multiple nanowrinkle regions across the sample, with wavelengths spanning from 1090 nm to 1170 nm (Fig. 1e). This spectral distribution is mostly associated with bilayer  $MoTe_2$  emission and could potentially be extended to longer wavelengths toward 2<sup>nd</sup> and 3<sup>rd</sup> telecom windows by exploiting multilayer  $MoTe_2$ . The observed narrow and linearly polarized emission lines from  $MoTe_2$  nanowrinkles indicate a potential single-photon emission. To verify this and further investigate their single-photon properties, we then perform systematic optical spectroscopy on the fabricated quantum emitters.

### III. SINGLE-PHOTON EMISSION

Fig. 2a presents  $\mu$ PL spectra ( $T \sim 4$  K) taken from a representative quantum emitter ( $QE_A$ ), collected with the polarizer aligned to maximize the emission signal (corresponding to the polarization axis with high DOLP). To investigate how the excitation energy affects the emission properties, we collected  $\mu$ PL spectra under two different excitation wavelengths of above-band 650 nm (orange, labeled AB) and quasi-resonant 1080 nm (blue, labeled QR). The quasi-resonant excitation results in a narrower emission line ( $\sim 230$   $\mu$ eV) with significantly suppressed background even under a longer integration time of 10 s, whereas the above-band excitation leads to broader emission ( $\sim 280$   $\mu$ eV) accompanied by strong, broad background emission. Moreover, when reducing

the integration time from 10 s to 1 s under quasi-resonant excitation, the emission linewidth narrows further to the resolution-limited value of  $\sim 150$   $\mu$ eV (see more details in Supporting Note S4). This significant narrowing under shorter integration time suggests strong spectral diffusion, which leads to severe inhomogeneous broadening due to an unstable charge environment.

To further evaluate the emitter response, we analyzed the PL intensity from  $QE_A$  as a function of excitation power (Fig. 2b, bottom panel). For both excitation schemes, the integrated PL intensity scales with excitation power with an exponent of approximately 1–1.1, consistent with the behavior of a single excitonic transition. It also suggests that higher excitation powers are required to reach saturation under above-band excitation compared to quasi-resonant. Additionally, the emission peak-to-background ratio (Fig. 2b, top panel) is consistently higher for quasi-resonant excitation, especially below saturation, indicating reduced background contribution and enhanced spectral purity. Under saturation conditions, quasi-resonant excitation also yields  $\sim 1.7$  times higher emission intensity than the above-band excitation. This enhancement likely results not only from the reduced excitation-emission detuning in the QR excitation, leading to more efficient excitation of the emitter, but also from improved optical alignment in our setup. Specifically, the cryogenic achromatic objective used in this experiment was not fully optimized to maintain identical excitation and collection conditions both at 650 nm and 1080 nm, which likely contributed to the reduced PL signal quality observed under the above-band excitation.

To investigate the recombination dynamics of these emitters, we performed time-resolved photoluminescence (TRPL) measurements under both pulsed above-band and quasi-resonant excitations with 80 MHz repetition rate. The TRPL trace of the delocalized exciton reveals an ultra-fast decay below 80 ps (Fig. 2c, dark red line), at the resolution limit of our setup, consistent with previous reports for TMDs-based delocalized excitonic transitions [44]. In contrast,  $QE_A$  exhibits slower decay as well as excitation-dependent dynamics. Under both the above-band (orange line) and quasi-resonant (blue line) excitations, we observed the fast decay of  $\tau = 440$ –450 ps. Moreover, the above-band excitation showed biexponential decay, with a slower component  $\tau_S = 2.4$  ns, suggesting additional non-radiative processes such as carrier trapping near the emitter. The quasi-resonant excitation revealed simpler recombination dynamics, in line with improved excitation conditions mentioned above. Additional TRPL measurements across the sample, summarized in Supporting Note S5, showed an average decay of 263 ps, with a range spanning from 130 ps to 440 ps.

From the measured lifetimes, we estimated the transform-limited linewidths ( $W_{\text{rad}} = h/(2\pi\tau)$ ) and compared them to the experimental emission linewidths ( $W_{\text{exp}}$ ) via the ratio  $R = W_{\text{exp}}/W_{\text{rad}}$  to quantify how close the emitter approaches the transform-limited regime ( $R = 1$ ) [41]. For the above-band excitation, using

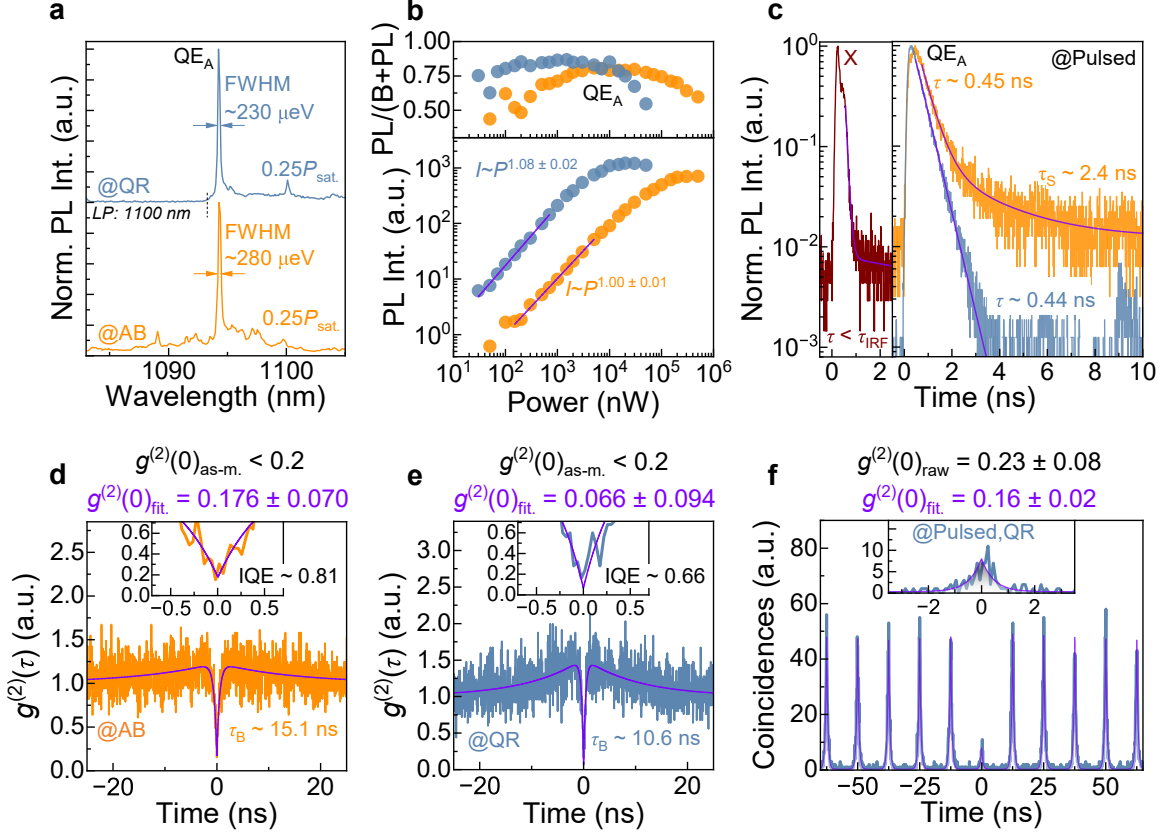


FIG. 2. **QE<sub>A</sub> emission characterization and comparison between above-band (AB, 650 nm, orange) and quasi-resonant (QR, 1080 nm, blue) excitation schemes (T ~ 4 K).** **a)** Normalized  $\mu$ PL spectra of QE<sub>A</sub> (~10 s integration time,  $0.25P_{\text{sat}}$ , CW). QR excitation yields a lower background and a narrower linewidth (230  $\mu\text{eV}$  vs 280  $\mu\text{eV}$ ). **b)** Top: PL-to-background ratio as a function of power (CW). QR excitation shows an improved PL-to-background ratio at low power and saturation, while AB shows an improved ratio for the saturation condition. Bottom: Saturation curves, both similar in shape (exponent between 1 and 1.1), but AB requires a higher power to saturate. **c)** TRPL traces under both excitation schemes (pulsed operation) and also from the delocalized exciton (dark red). The broad unlocalized excitonic transition decays rapidly (~80 ps), limited by the IRF. AB excitation yields a biexponential decay ( $\tau \sim 450$  ps,  $\tau_S \sim 2.4$  ns), whereas QR yields a clean monoexponential decay with  $\tau \sim 440$  ps for QE<sub>A</sub>. **d)** Second-order autocorrelation measurement ( $g^{(2)}(\tau)$ ) under CW AB excitation. Some bunching is observed, the fit yields a bunching time of  $\tau_B \sim 15.1$  ns. The inset presents the antibunching dip around a limited time window ( $\pm 1.5$  ns) and a fitted value of  $g^{(2)}(0) = 0.176 \pm 0.070$ . **e)**  $g^{(2)}(\tau)$  under CW QR excitation. A more pronounced bunching is observed with a calculated  $\tau_B \sim 10.6$  ns. The inset showing the antibunching dip ( $\pm 1.5$  ns) reveals a fitted  $g^{(2)}(0) = 0.066 \pm 0.094$ . **f)** Pulsed QR  $g^{(2)}(\tau)$  within a measurement window of  $\pm 60$  ns, with no observable bunching. The inset ( $\pm 4$  ns) presents the zero-delay peak with fitted value of  $g^{(2)}(0) = 0.16 \pm 0.02$ .

the fast decay component, we obtained  $W_{\text{rad}} \sim 1.46 \mu\text{eV}$  and  $W_{\text{exp}} = 280 \mu\text{eV}$ , yielding  $R_{AB} = 192$ . Similarly, for the quasi-resonant excitation,  $W_{\text{rad}} \sim 1.497 \mu\text{eV}$  and  $W_{\text{exp}} = 230 \mu\text{eV}$  give  $R_{QR} = 154$ , while using  $W_{\text{exp}, 1s} = 150 \mu\text{eV}$  the ratio decrease to  $R_{QR} = 100$ . This reduction likely results from better excitation in the quasi-resonant case, improving linewidth and from shorter integration time, limiting the impact of spectral diffusion. The  $R \geq 100$  values still indicate significant broadening related to additional dephasing, reducing coherence and photon indistinguishability. However, these values are already comparable to the best reported value for non-cavity-enhanced TMD-based QEs [41]. The comparatively low  $R$  values primarily reflect the intrinsically

short lifetimes of our emitters, which are nonetheless consistent with previous studies on MoSe<sub>2</sub> studies [46].

To complete the optical characterization of QE<sub>A</sub>, we performed second-order autocorrelation measurements under CW both above-band (Fig. 2d) and quasi-resonant (Fig. 2e) excitations. In both cases, the measured raw  $g^{(2)}(0)$  values below 0.2 indicate strong photon antibunching. Fitting the data yields  $g^{(2)}(0) = 0.176 \pm 0.070$  for above-band and  $0.066 \pm 0.094$  for quasi-resonant, confirming the single-photon nature of the emission from QE<sub>A</sub>. Beyond emission purity, the  $g^{(2)}(\tau)$  measurements also offer insight into the emitter internal dynamics. Under both CW excitation schemes, we observed bunching around the central antibunching dip, typically attributed



to blinking behavior on timescales within a measurement window (here  $\pm 1$   $\mu$ s). Including this additional dynamics in the fit, we extracted bunching times of  $\sim 15.1$  ns for above-band and  $\sim 10.6$  ns for quasi-resonant excitation. These values, along with the extracted on/off decay times ( $\tau_{\text{on}}/\tau_{\text{off}} = 78$  ns/19 ns for above-band and 31 ns/16 ns for quasi-resonant), reflect the influence of non-radiative processes contributing to the bunching dynamics. We attribute the observed blinking to several possible mechanisms. A primary contributor is spectral diffusion, where charge fluctuations in the local environment cause emission energy shifts. If spectral filtering is narrow, this can lead to intermittent signal detection. Additionally, nearby defect states may transiently trap charge carriers, reducing the excitation efficiency and thus affecting the emitter recombination dynamics. These processes can also modulate the relative populations of excitonic species, resulting in temporal switching between neutral and charged exciton configurations. Despite their distinct origins, all these mechanisms reduce the internal quantum efficiency (IQE) by rendering the emitter inactive during “off” intervals. From the fitted bunching amplitudes in the autocorrelation data, we estimated IQEs of  $\sim 0.81$  and  $\sim 0.66$  under CW above-band and quasi-resonant excitations, respectively. This highlights the relative advantage of above-band excitation in suppressing non-radiative channels and stabilizing emission. Furthermore, power-dependent second-order autocorrelation measurements under CW quasi-resonant excitation (Supporting Note S4) reveal reduced bunching - and thus higher IQE - at elevated excitation powers. This behavior is likely linked to saturation of nearby charge traps, providing additional evidence for the key role of charge fluctuations and its dependence on excitation conditions.

In addition to CW excitation, we performed second-order correlation measurements under quasi-resonant pulsed excitation (Fig. 2f). The raw data analysis yields a  $g^{(2)}(0) = 0.23 \pm 0.08$ , based on comparing the zero-delay peak area to the average side peaks. A fit to the autocorrelation histogram yields a slightly lower value of  $g^{(2)}(0) = 0.16 \pm 0.02$ . To understand the origin of these nonzero values, we compared the measurements to theoretical  $g^{(2)}(0)$  of an ideal single-photon emitter with background emission [47], using the measured signal-to-background ratios. For CW above-band excitation, the background alone limits  $g^{(2)}(0)$  to  $\sim 0.19$ , while for both CW and pulsed quasi-resonant excitations, the corresponding ratios predict values of  $\sim 0.06$  and  $\sim 0.12$ , respectively. These estimates are consistent with our data, confirming that background emission plays a dominant role and  $\text{QE}_A$  exhibits near-unity single-photon purity.

The pulsed  $g^{(2)}(\tau)$  histogram from (Fig. 2f), acquired during the same cooldown as the CW data, shows no observable bunching. However, a second dataset from a different cooldown (Supporting Note S6) reveals clear bunching under pulsed excitation. This suggests the presence of blinking dynamics and reduced internal quantum efficiency, which were likely masked in Fig. 2f due

to limited coincidence statistics. Differences in the local charge environment between cooldowns may also contribute to the observed variation in bunching amplitude. Despite these variations, all measurements confirm the single-photon nature of  $\text{QE}_A$ ’s emission. The emitter displays highly pure and strongly polarized quantum light, with a sub-nanosecond lifetime, marking it as a high-quality single-photon source.

To demonstrate the reproducibility of our fabrication method, we also characterized handful number of quantum emitters from other wrinkled sites within the same sample (Supporting Note S7) and in other samples fabricated with the same method (Supporting Note S8). As summarized in Supporting Notes S5, S7, and S8, these emitters exhibit similar optical properties, including reproducible narrow emission lines, high DOLP, short lifetimes, and high-purity single-photon emission, further confirming the robustness and scalability of our fabrication approach. In the following section, we turn to the characterization of a second quantum emitter embedded in a fully hexagonal boron nitride (hBN)-encapsulated heterostructure, enabling direct comparison with the bare bilayer  $\text{MoTe}_2$  system discussed thus far.

#### IV. HBN-ENCAPSULATION

Using a similar characterization approach, we investigated fully hBN-encapsulated bilayer  $\text{MoTe}_2$  quantum emitters to study the impact of additional dielectric screening [20, 40, 41, 48–51] and modified strain landscape, specifically, the bubble-like morphology induced by encapsulation (see Supporting Note S1).

Figure 3a shows a representative  $\mu$ PL spectrum from  $\text{QE}_{\text{hBN}}$  under CW quasi-resonant excitation. More examples are presented in Supporting Note S9. Gaussian fitting yields a linewidth of  $\sim 350$   $\mu$ eV (1 s integration:  $\sim 280$   $\mu$ eV). Statistical analysis confirms a modest overall linewidth increase, ranging from 180  $\mu$ eV to 750  $\mu$ eV (see Supporting Note S5). This slight broadening likely arises from weaker strain due to the rigidity of hBN [36, 52], which promotes bubble formation and possibly shallower confinement, increasing sensitivity to charge noise.

Polarization-resolved PL measurements (Fig. 3b,c) for  $\text{QE}_{\text{hBN}}$  reveal markedly reduced degrees of linear polarization (DOLP  $\sim 14\%$ ) compared to unencapsulated emitters, consistent with smaller confinement asymmetry. Two correlated peaks display an energy splitting of  $\sim 300$ – $500$   $\mu$ eV, indicative of fine-structure splitting (FSS). Residual spectral wandering limits precise characterization, but the orthogonal polarization dependence confirms two exciton states with perpendicular dipole orientations. Similar FSS values ( $\sim 300$   $\mu$ eV to  $\sim 1200$   $\mu$ eV) are observed for other encapsulated emitters (Supporting Notes S5, S9). In contrast, unencapsulated emitters subjected to stronger wrinkle-induced strain exhibit larger FSS and more imbalanced emission intensities, consistent with stronger anisotropic confinement (Supporting Notes

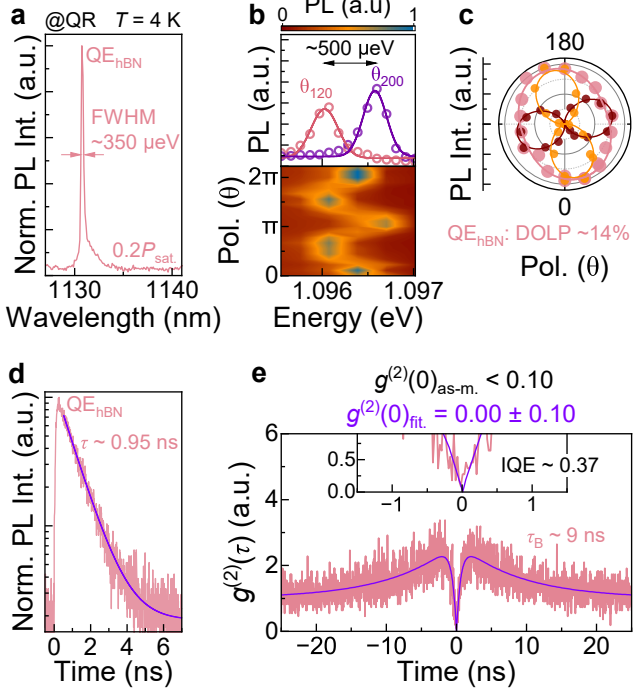


FIG. 3. **hBN-encapsulated quantum emitter ( $QE_{hBN}$ ) at  $T \sim 4$  K under QR excitation.** **a)** Normalized  $\mu$ PL spectrum recorded under CW excitation ( $\sim 10$  s integration time,  $0.2P_{sat}$  excitation power). A Gaussian fit yields a linewidth of  $\sim 350$   $\mu$ eV. **b)** The top panel shows  $\mu$ PL spectra measured at orthogonal polarization angles of  $120^\circ$  (pink) and  $200^\circ$  (purple), highlighting the fine structure splitting of  $\sim 500$   $\mu$ eV. The bottom panel depicts a polarization-dependent  $QE_{hBN}$  emission color map with the detection polarization angle varied from 0 to  $400^\circ$ . **c)** Polarization profiles of the individual peaks' intensity (orange and dark red) and their combined emission (pink). The two peaks exhibit strong linear polarization oriented nearly perpendicular to each other, while the combined emission shows a reduced degree of linear polarization (DOLP  $\sim 14\%$ ). **d)** TRPL measurement under pulsed excitation. A monoexponential fit reveals a decay time of  $\tau \sim 950$  ps. **e)** Second-order correlation measurement ( $g^{(2)}(\tau)$ ) under CW excitation. The data show clear bunching around the antibunching dip, with a fitted bunching time of  $\tau_B \sim 9$  ns. The inset displays the central region ( $\pm 1.5$  ns), where the fit yields  $g^{(2)}(0) = 0.00 \pm 0.01$ .

S10). The majority of unencapsulated emitters display FSS only under applied bias, suggesting that many are initially charged excitons where splitting is not present, while external fields favor neutral excitonic states that reveal the underlying FSS.

Time-resolved PL measurements under pulsed quasi-resonant excitation (Fig. 3d) show a decay time of  $\tau \sim 950$  ps for  $QE_{hBN}$ . Across multiple emitters, lifetimes average 600 ps, with a range of  $\sim 190$ – $1000$  ps (Supporting Notes S5, S9). Compared to unencapsulated emitters ( $\tau \sim 263$  ps), encapsulated QEs exhibit significantly longer lifetimes, likely due to weaker strain confinement,

reduced exciton localization, and thus lower oscillator strength. Non-radiative contributions appear less significant, as encapsulated and unencapsulated emitters display comparable PL intensities. To assess proximity to the transform-limited regime, we calculated the corresponding  $R_{hBN} \sim 505$ , using the measured linewidth (350  $\mu$ eV) and lifetime of 950 ps. This value is substantially higher than both  $R_{AB}$  and  $R_{QE}$ , yet remains comparable to state-of-the-art reports [41]. The increased  $R$  primarily results from longer radiative lifetimes rather than intrinsic linewidth broadening, consistent with weaker confinement.

Second-order correlation measurements under CW quasi-resonant excitation confirm the single-photon nature of  $QE_{hBN}$ , yielding a raw  $g^{(2)}(0) < 0.1$  and a fitted value of  $0.00 \pm 0.10$  (Fig. 3e). Strong photon bunching is observed with a bunching time of  $\sim 9$  ns. Direct fitting of the on-off processes' timescales yields  $\tau_{on}/\tau_{off} = 14$  ns/24 ns, from which the IQE can be estimated at  $\sim 0.37$ . The reduced IQE, relative to unencapsulated emitters, suggests a greater contribution from non-radiative processes and blinking, consistent with the slightly broader linewidths. Fluctuations in the local charge environment likely exacerbate these effects, as indicated by the significant line wandering observed in both platforms (Supporting Notes S4, S9). Overall, the results demonstrate that stable single-photon emission can be reliably achieved from QEs in both encapsulated and unencapsulated bilayer  $MoTe_2$ . Encapsulation modifies the strain landscape, polarization properties, and recombination dynamics, while local charge fluctuations remain a dominant source of blinking and spectral instability. In the next section, we investigate how applying an external electric field can mitigate these effects and enhance emission stability.

## V. ELECTRICAL TUNING

To explore the effect of an external electric field, we systematically investigated how electrical biasing modifies the charge environment and, consequently, the optical properties of the quantum emitters. Figure 4a illustrates the device, where the  $MoTe_2$  flake contacts one electrode while a second, nearby electrode remains isolated to prevent short-circuiting and direct current flow. Figure 4b presents the bias-dependent  $\mu$ PL response of the exemplary emitter  $QE_A$  (bottom panel) under CW quasi-resonant excitation. As  $V_{bias}$  increases from  $-2$  V to  $+15$  V, the main emission line exhibits a clear red-shift starting near  $V_{bias} = +4$  V, consistent with a linear Stark effect. The total tuning range exceeds 3 nm ( $\sim 3$  meV), enabling spectral alignment of an emission line to another individual emission line as demonstrated in Fig. 4c. This tunability is essential for quantum photonic applications requiring indistinguishable photons from spatially separated sources. Interestingly, the Stark response is strongly polarity-dependent: positive bias enhances PL

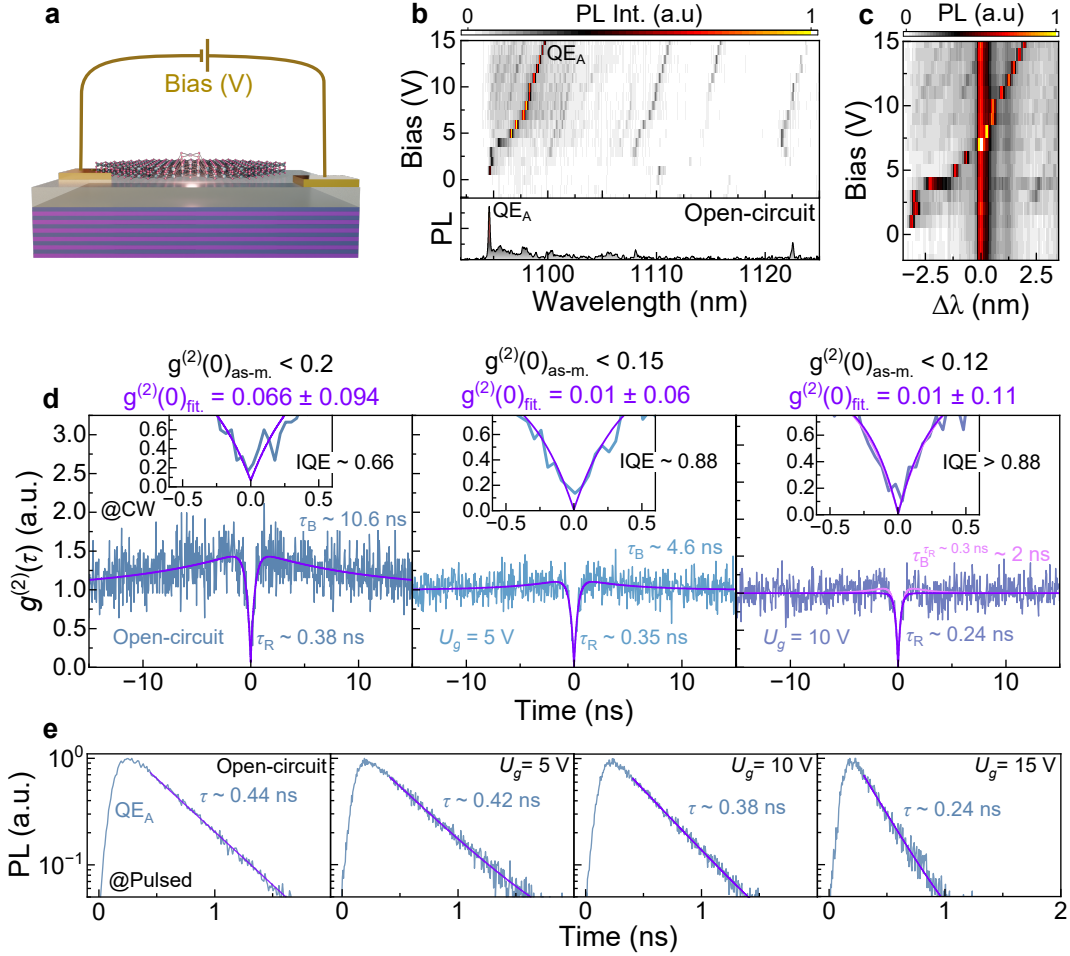


FIG. 4. **Effects of biasing on the  $QE_A$  optical properties under CW and pulsed QR excitation at  $T \sim 4$  K.** **a)** Schematic of the device structure, showing bilayer  $MoTe_2$  in contact with one gold electrode and near another, both connected to a voltage source. **b)** The bottom panel shows a  $\mu$ PL spectrum (CW) of  $QE_A$  at open-circuit condition, revealing additional but much weaker emission from other lines. In the top panel, we have the bias-dependent evolution of the same spectral range from  $-2$  V to  $+15$  V. Emission quenches under negative bias, while increasing bias results in intensity enhancement and a clear redshift of  $QE_A$  and nearby peaks due to the Stark shift effect. **c)** Overlay of the bias-tuned  $QE_A$  PL map with a reference emitter of similar emission energy at open-circuit. As the bias increases,  $QE_A$  tunes across the reference peak, demonstrating the possibility of bias-driven spectral matching between distinct single-photon sources. **d)** CW QR second-order autocorrelation measurements of  $QE_A$  line at open circuit,  $+5$  V, and  $+10$  V. With increasing bias, bunching becomes less pronounced, indicating improved internal quantum efficiency and blinking reduction. Extracted bunching times decrease from  $\tau_B \sim 10.6$  ns to  $\sim 4.6$  ns to  $\sim 2.0$  ns, with the corresponding rising times following suit at  $\tau_R \sim 380$  ps,  $\sim 350$  ps, and  $\sim 240$  ps, respectively. Insets ( $\pm 0.5$  ns) show antibunching dips, with the fitted  $g^{(2)}(0)$  improving from  $0.066 \pm 0.094$  (0 V) to  $0.01 \pm 0.06$  ( $+5$  V) and  $0.01 \pm 0.11$  ( $+10$  V). **e)** Normalized TRPL measurements of  $QE_A$  (pulsed excitation) under four bias configurations (open-circuit,  $+5$  V,  $+10$  V,  $+15$  V). As the bias increases, we observed decreasing decay times, with the monoexponential fits yielding  $\sim 440$  ps,  $\sim 420$  ps,  $\sim 380$  ps, and  $\sim 240$  ps for 0 V,  $+5$  V,  $+10$  V, and  $+15$  V, respectively.

intensity and induces tunability, while negative bias suppresses emission without a significant spectral shift. Occasionally, abrupt step-like switching between two emission lines is observed near  $V_{bias} = +4$  V, likely caused by changes in the local charge environment and formation of different excitonic complexes (see more detailed analysis in Supporting Note S11). By measuring the experimental linewidth of  $QE_A$  under various bias voltages (Supporting Note S10), we observed only negligible variation, with  $W_{exp}$  remaining stable  $\sim 150$   $\mu$ eV (0.5 s integration time,

see more details in Supporting Note S11). However, because these linewidths are already close to the resolution limit of our setup ( $\sim 140$ - $160$   $\mu$ eV), the measured values may underestimate the true spectral width.

Biasing also influences recombination dynamics and single-photon purity. Second-order autocorrelation measurements in Figure 4d show steady reduction in  $g^{(2)}(0)$  from  $0.066 \pm 0.094$  to  $0.01 \pm 0.06$  at  $+5$  V and  $0.01 \pm 0.11$  and at  $+10$  V. The suppression of photon bunching indicates reduced blinking, reflected in improved IQE, in-

creasing from  $\sim 0.66$  to  $\sim 0.87$  at  $+5$  V and approaching unity at  $+10$  V. These results confirm that biasing stabilizes the emission, suppresses non-radiative losses, and enhances single-photon purity. Time-resolved PL measurements (Fig. 4e) reveal a pronounced reduction in lifetime from  $\sim 440$  ps at 0 V to  $\sim 240$  ps at  $+15$  V, more than 45% decrease consistent with prior observations [41]. Since the measured linewidths remain resolution-limited ( $\sim 150$   $\mu$ eV), the corresponding linewidth-to-lifetime ratio  $R$  decreases from  $R_{0V} = 100$  to  $R_{15V} = 55$ , approaching the transform-limited regime. To our knowledge, this represents one of the lowest reported  $R$  values for comparable TMD-based systems [41], highlighting the potential of electrical control to improve emitter coherence. The observed reduction in lifetime is unlikely due to enhanced non-radiative recombination, as PL intensities remain stable across biases. Instead, we attribute it to a bias-induced modulation of the oscillator strength: the applied electric field partially screens the built-in potential separating carriers, increasing electron-hole wavefunction overlap and thus radiative recombination rates. Similar lifetimes are found across different emitters (Supporting Figure S5), reinforcing this interpretation. Overall, electrical biasing provides robust control over both the emission energy and radiative dynamics of MoTe<sub>2</sub> quantum emitters. We demonstrate Stark tuning exceeding  $\sim 3$  meV, suppression of long-timescale blinking, improved single-photon purity, and a near-halving of  $R$  towards the transform limit. However, within our spectral resolution, we observe no significant suppression of fast spectral diffusion, consistent with the intrinsically low charge noise of the MoTe<sub>2</sub> bilayer. Having established the fundamental optical properties of our emitters under bare, encapsulated, and electrically biased conditions, we now turn to photon indistinguishability, which is a key benchmark for quantum photonic technologies and the biggest challenge in the TMD-based quantum emitters.

## VI. PHOTON INDISTINGUISHABILITY

Before performing Hong-Ou-Mandel (HOM) measurements, we revalidated the properties of QE<sub>A</sub> after a second cooldown to ensure stability following exposure to ambient conditions. Since the sample had been exposed to ambient conditions between measurements, this step ensured that the emitter's characteristics remained stable. Under pulsed quasi-resonant excitation, matching the HOM experimental settings, QE<sub>A</sub> maintained single-photon emission, with a fitted  $g^{(2)}(0)$  value below 0.35, despite some increase in bunching and reexcitation signature due to the higher excitation power used to improve count rates (Supporting Note S6).

We then investigated two-photon interference using a custom HOM interferometer [53] under pulsed quasi-resonant excitation (80 MHz), with a delay line of 12.5 ns, using co-polarized and cross-polarized configurations for the interferometer arms. Figure 5a presents the HOM

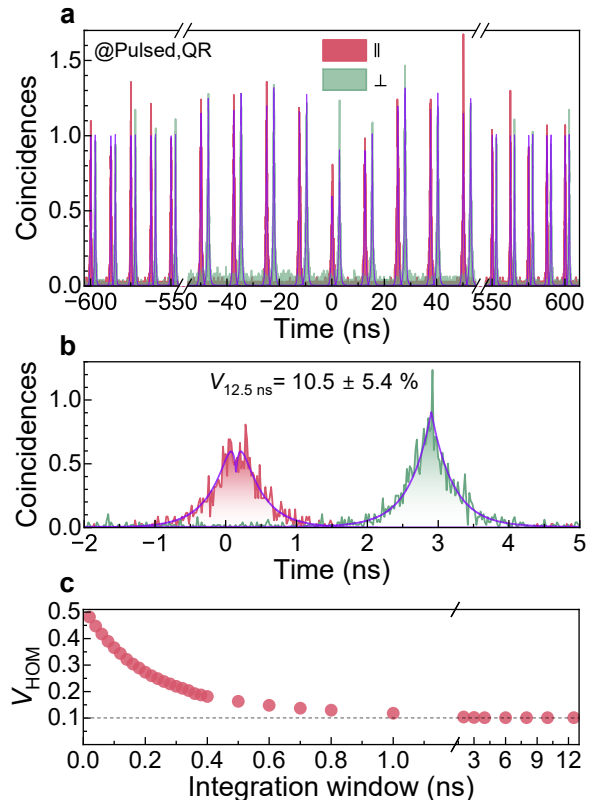


**FIG. 5. Two-photon interference HOM measurement under pulsed QR excitation at  $\sim 4$  K.** **a)** The HOM measurements for both polarization configurations (co-polarized configuration: red line, cross-polarized configuration: green line). For clarity, the cross-polarized data are slightly time-shifted to enhance visual distinction. The data are presented over a wide time range ( $\pm 600$  ns) out of the bunching region. Purple lines indicate the fits for both configurations, including bunching observed close to the zero-delay region. **b)** Magnified plot of the zero-delay peak showing a direct difference between co- and cross-polarized configurations. A comparison of the integrated coincidences in 12.5 ns time integration window for both configurations indicates  $V_{12.5 \text{ ns}} = 10.4 \pm 5.4 \%$ . **c)** Calculated visibility of two-photon interference for different time integration windows. The data shows visibility values higher than  $\sim 30\%$  for reduced integration windows below 200 ps, while longer time windows feature a reduction in visibility, which saturates at longer time scales.

measurements for both polarization configurations over a wide time range ( $\pm 600$  ns), with the cross-polarized data slightly time-shifted for clarity. We deliberately include this extended time window to display coincidence peaks that are temporally distant from the zero-delay region and thus unaffected by bunching. These outer peaks serve as a reliable reference for normalization, ensuring that the bunching near zero-delay does not bias the normalization process. We fitted the raw HOM data using a standard model for pulsed two-photon interference [53, 54], which includes an additional bunching component to account for residual photon correlations at longer

timescales [54]. The slight asymmetry of our first two side-peaks (delay:  $\pm 12.5$  ns) is interpreted as a consequence of the modest imbalance between the two arms of our second fiber-based beamsplitter with optimal wavelength range  $930 \pm 100$  nm. Figure 5b shows a magnified view around zero delay, where the integrated peak areas yield an HOM visibility of  $V_{12.5\text{ ns}} = 10.5 \pm 5.4\%$  using a full 12.5 ns integration window. Importantly, temporal filtering reveals significantly higher visibilities: values exceed  $>30\%$  with post-selection by temporal filtering, restricting the integration window to below 200 ps (Fig. 5c). For longer integration windows, the visibility gradually decreases and saturates near  $\sim 10\%$ . A comprehensive robustness analysis of these results is provided in Supporting Note S12.

From the HOM fitting procedure, we also estimate the emitter's coherence time to be  $\tau_c = 63 \pm 12$  ps, though this value is partly limited by our setup resolution, signal-to-noise ratio, and reduced indistinguishability. Compared to the measured radiative lifetime ( $\tau \sim 240$ -440 ps), this short coherence time explains the modest interference visibility. Additionally, the elevated  $g^{(2)}(0)$  under higher-power excitation likely contributes to the reduced indistinguishability, consistent with the strong dependence of visibility on the integration window. Despite these limitations, our results demonstrate HOM interference with a visibility of  $\sim 10\%$ , increasing to  $>30\%$  with post-selection temporal filtering. To the best of our knowledge, this represents the highest reported indistinguishability for any 2D TMD-based quantum emitter and the first such demonstration for MoTe<sub>2</sub>.

## VII. DISCUSSION

Our results demonstrate reproducible generation and comprehensive optical characterization of single-photon emitters (QEs) hosted in bilayer MoTe<sub>2</sub> within the near-infrared spectral range (1090–1200 nm). Using a combined approach of strain engineering via nanopillars and controlled e-beam-induced defect activation, we established a robust process for realizing deterministic MoTe<sub>2</sub>-based quantum emitters. These emitters exhibit narrow linewidths down to  $\sim 150$   $\mu\text{eV}$ , short radiative lifetime as short as  $\sim 130$  ps, and high single-photon purity with  $g^{(2)}(0) < 0.2$  under various excitation conditions. We investigated the impact of hBN encapsulation and electrical biasing on the optical properties. Encapsulation leads to modified strain landscapes and induces FSS down to  $\sim 300$   $\mu\text{eV}$ , in contrast to larger splittings (1.8-2.2 meV) in unencapsulated emitters where wrinkle-induced anisotropic strain dominates. Electrical biasing, on the other hand, enables continuous Stark tuning over  $\sim 3$  meV, offering a path toward remote quantum interference between individual emitters. Importantly, we observed bias-induced suppression of blinking and a reduction of the linewidth-to-lifetime ratio down to  $R \sim 55$ , approaching state-of-the-art performance for TMD-based

QEs even without cavity integration.

While the emitters studied here predominantly emit in the 1090-1200 nm range, earlier work has reported MoTe<sub>2</sub>-based emitters extending into the telecom band up to 1550 nm [42]. In our current experiments, thicker MoTe<sub>2</sub> flakes exhibit broader, less localized emission features at longer wavelengths, suggesting that achieving a sharp, stable emitter in the telecom regime may require further optimization of strain engineering, defect formation, and dielectric environment control. Exploring these design parameters in thicker flakes represents a promising direction toward extending MoTe<sub>2</sub>-based single-photon sources into the telecom range, which is highly relevant for fiber-based quantum communication. Compared to the only previous report on MoTe<sub>2</sub> quantum emitters [42], our emitters exhibit significantly narrower linewidths (150-300  $\mu\text{eV}$  vs.  $\sim 600$   $\mu\text{eV}$ ) and much shorter lifetimes (130-440 ps vs.  $>20$  ns). This discrepancy likely arises from differences in oscillator strength related to strain profiles and confinement regimes or from the impact of additional charge trapping processes rather than purely non-radiative effects, as we observed no significant drop in emission brightness even for the fastest emitters. The short lifetimes are consistent with the spin-allowed bright exciton ground state characteristic of Mo-based TMDs [7, 55], similar to previous observations in MoSe<sub>2</sub> emitters [46].

The main finding of this study is the demonstration of HOM interference between consecutively emitted photons from a single MoTe<sub>2</sub> quantum emitter. We achieved a visibility of  $\sim 10\%$  within a 12.5 ns integration window and exceeding  $\sim 30\%$  with sub-200 ps post-selection temporal filtering. To the best of our knowledge, this represents the highest reported indistinguishability for any 2D TMD-based QE to date and the first such demonstration for the MoTe<sub>2</sub> platform in the near-infrared range. These results underline the potential of MoTe<sub>2</sub> quantum emitters for scalable quantum photonic applications, especially those targeting telecom-adjacent wavelengths. Despite these advances, photon indistinguishability remains limited by decoherence effects, likely driven by phonon coupling and charge noise. Our HOM measurements reveal a strong dependence of visibility on time filtering, consistent with recent theoretical predictions [56, 57]. Achieving indistinguishability beyond 50% will likely require integration with high-Q photonic structures to exploit Purcell enhancement [18, 30, 32, 33, 43, 58, 59] and enhancement of the zero-phonon emission line and the implementation of advanced excitation schemes, such as resonant excitation, swing-up of quantum emitter population (SUPER), or phonon-assisted excitation, to improve brightness and coherence of these emitters [12, 35, 37, 38, 56].

In summary, we demonstrate a reproducible approach for realizing high-quality, tunable quantum emitters in bilayer MoTe<sub>2</sub>, achieving narrow linewidths, fast radiative decay, high single-photon purity, and promising photon indistinguishability. Most notably, we report the



first observation of two-photon interference from MoTe<sub>2</sub>-based quantum emitters, marking a significant step toward scalable, near-infrared single-photon sources for applications in quantum technologies.

## VIII. METHODS

### A. Sample preparation

*Substrate fabrication:* The substrate consists of a distributed Bragg reflector (DBR) with alternating layers of GaAs and AlAs, fabricated by low-pressure metalorganic vapor-phase epitaxy (MOVPE). On top of the DBR, a 110 nm thick Al<sub>2</sub>O<sub>3</sub> layer was deposited via atomic layer deposition (ALD) at 200 °C, providing electrical insulation and surface passivation. Alignment marks and electrodes were fabricated by spin coating and patterning UV resist (nLOF 2020, AZ), followed by physical vapor deposition of a Ti/Au/Ti multilayer (5/50/5 nm) and a liftoff process.

*Nanopillar fabrication:* To fabricate the nanopillars, a small chip was cleaved from the wafer and spin-coated with high-resolution negative electron-beam resist (hydrogen silsesquioxane, HSQ; XR-1541-006, Dow Corning) at 2000 rpm for 1 minute. The coated sample underwent a two-step bake at 120 °C and 220 °C, each for 2 minutes. Nanopillars in the shape of three-pointed stars, ~80 nm tall, were patterned using electron-beam lithography (JBX-9500FS, JEOL, 100 kV, 6 nA) with a dose of 11000  $\mu\text{C}/\text{cm}^2$  and developed in a 1:3 AZ 400K:H<sub>2</sub>O solution.

*Exfoliation & Transferring:* MoTe<sub>2</sub> flakes were exfoliated from bulk crystals (HQ Graphene) onto PDMS films prepared on glass slides, via the established scotch-tape technique [60]. Their thicknesses were confirmed via room-temperature photoluminescence (PL) under 650 nm LED excitation using an optical microscope (Nikon 50 $\times$ , NA = 0.8). For the encapsulated samples, hexagonal Boron Nitride (hBN) flakes (3–8 layers) were prepared using the same exfoliation process and identified through an optical microscope (Nikon 20 $\times$ , NA = 0.45). The transferring of the flakes was performed with the help of a transfer stage that could heat the substrate to ~70 °C, enabling the van der Waals forces to overcome PDMS adhesion, thus releasing the flakes onto the substrate.

*Defect fabrication:* Defects were introduced to the lattice by electron-beam bombardment (JBX-9500FS, JEOL, 100 kV, 1000  $\mu\text{C}/\text{cm}^2$ ) of the strained areas.

*Sample reproducibility:* To investigate the reproducibility of the QEs' fabrication, additional samples were produced utilizing an identical sample fabrication method (more details in Supporting Note S8). Moreover, the application of the full hBN encapsulation as well as the SiO<sub>2</sub>/Si substrate was investigated to verify the potential impact of a different dielectric environment.

### B. Optical characterization

All optical measurements of the samples were obtained with the help of a custom-built low-temperature micro-photoluminescence ( $\mu\text{PL}$ ) setup. The sample was mounted inside a closed-cycle cryostat (attoDRY800xs, Attocube) operating at a base temperature of ~4 K. The cryostat was equipped with piezoelectric nanopositioners for precise spatial alignment and a high-numerical-aperture microscope objective (60 $\times$ , NA = 0.8, LT-APO/Telecom, Attocube) integrated within the cryostat chamber to facilitate efficient collection of the photoluminescence signal. Excitation of the quantum emitters was performed using two types of semiconductor diode lasers (PicoQuant): an above-band laser at 650 nm (LDH-D-C-650) and a quasi-resonant laser at 1080 nm (LDH-D-C-1080). Both lasers operated in continuous-wave (CW) or pulsed modes, delivering pulses shorter than 100 ps with adjustable repetition rates ranging from 2.5 to 80 MHz.  $\mu\text{PL}$  spectra were acquired using a spectrometer based on a 0.328 m focal-length monochromator (Kymera 328i, Andor, Oxford Instruments) equipped with interchangeable gratings (150, 600, and 830 lines/mm) and a deep thermo-electrically cooled (In,Ga)As linear array detector (iDus 1.7  $\mu\text{m}$ , Andor, Oxford Instruments), providing a maximum spectral resolution of ~140-160  $\mu\text{eV}$ . Time-resolved PL characterization and single-photon statistics measurements were performed via time-correlated single-photon-counting mode. To verify single-photon emission, a Hanbury Brown and Twiss (HBT) configuration employing a 50:50 fiber beamsplitter was used. Photon indistinguishability was assessed via Hong–Ou–Mandel (HOM) interference, utilizing a free-space beamsplitter (Wollaston prisms), a half-wave plate for polarization rotation in one arm, a second fiber-based beamsplitter, and a tunable optical delay line implemented via a combination of fiber and a linear translation stage. A three-paddle fiber polarization controller was employed for interferometer calibration. Detection was carried out using superconducting nanowire single-photon detectors (SNSPDs; ID281, ID Quantique) connected to a high-resolution single-photon counting module (Time Tagger Ultra, Swabian Instruments). Polarization-resolved PL measurements were performed using a rotating half-wave plate followed by a linear polarizer.

### C. Optical simulation

To estimate the extraction efficiency presented in Fig. 1b, we model the QE as a classical point dipole with in-plane orientation and harmonic time dependence at frequency  $\omega$ . The corresponding current density is  $\mathbf{J}(\mathbf{r}) = -i\omega\mathbf{p}\delta(\mathbf{r} - \mathbf{r}_d)$ , where  $\mathbf{r}_d$  is the position of the QEs and  $\mathbf{p}$  is the dipole moment. We then use the method described in the Supplementary Information of Ref. [61] to solve Maxwell's equation in the frequency domain.

## DATA AVAILABILITY

The data supporting the findings of this study are available within the main manuscript and its supplementary information files. Additional data are available from the corresponding authors upon reasonable request.

## ACKNOWLEDGEMENTS

The authors acknowledge support from the European Research Council (ERC-StG “TuneTMD”, grant no. 101076437) and the Villum Foundation (grant no. VIL53033). CR acknowledges the Danish National Research Foundation (grant no. DNRF147 NanoPhoton). BM and CR acknowledge the European Union’s Horizon Europe Research and Innovation Programme under the project QPIC 1550 (grant no. 101135785). The authors acknowledge E. Semenova for her support in the growth of the substrate. The authors also acknowledge the European Research Council (ERC-CoG “Unity”, grant no. 865230) and the cleanroom facilities at the Danish Na-

tional Centre for Nano Fabrication and Characterization (DTU Nanolab).

## AUTHOR CONTRIBUTIONS

AP and PM fabricated the MoTe<sub>2</sub> quantum emitters on the substrates and processed the samples. CR grew the substrate, including a distributed Bragg reflector. PW and AP performed the optical characterization of quantum emitters. PW performed the data analysis and processing of all the data. MJ performed calculations on the optical properties of the photonic structure. BM supervised and coordinated the project. PW, AP, PM, MJ, NG, and BM wrote the manuscript with the input of all co-authors.

## COMPETING INTERESTS

The authors declare no competing interest.

- 
- [1] D. A. Vajner, L. Rickert, T. Gao, K. Kaymazlar, and T. Heindel, *Adv. Quantum Technol.* **5**, 2100116 (2022).
  - [2] N. Maring, A. Fyrrillas, M. Pont, E. Ivanov, P. Stepanov, N. Margaria, W. Hease, A. Pishchagin, A. Lemaitre, I. Sagnes, T. H. Au, S. Boissier, E. Bertasi, A. Baert, M. Valdivia, M. Billard, O. Acar, A. Briussel, R. Mezher, S. C. Wein, A. Salavrakos, P. Sinnott, D. A. Fioretto, P.-E. Emeriau, N. Belabas, S. Mansfield, P. Senellart, J. Senellart, and N. Somaschi, *Nat. Photon.* **18**, 603 (2024).
  - [3] Y. Yu, S. Liu, C.-M. Lee, P. Michler, S. Reitzenstein, K. Srinivasan, E. Waks, and J. Liu, *Nat. Nanotechnol.* **18**, 1389 (2023).
  - [4] P. Holewa, A. Reiserer, T. Heindel, S. Sanguinetti, A. Huck, and E. Semenova, *Nanophotonics* **14**, 1729 (2025).
  - [5] T. Gao, M. von Helversen, C. Antón-Solanas, C. Schneider, and T. Heindel, *npj 2D Mater. Appl.* **7**, 4 (2023).
  - [6] M. Brotons-Gisbert, J. P. Martínez-Pastor, G. C. Ballessteros, B. D. Gerardot, and J. F. Sánchez-Royo, *Nanophotonics* **7**, 253 (2018).
  - [7] G. Wang, A. Chernikov, M. M. Glazov, T. F. Heinz, X. Marie, T. Amand, and B. Urbaszek, *Rev. Mod. Phys.* **90**, 021001 (2018).
  - [8] M. Stührenberg, B. Munkhbat, D. G. Baranov, J. Cuadra, A. B. Yankovich, T. J. Antosiewicz, E. Olsson, and T. Shegai, *Nano Lett.* **18**, 5938 (2018).
  - [9] F. Schröder, P. Wyborski, M. Xiong, G. Kountouris, B. Munkhbat, M. Wubs, P. T. Kristensen, J. Mørk, and N. Stenger, Strong coupling between a dielectric nanocavity and a monolayer transition metal dichalcogenide (2025), arXiv:2502.06529 [physics.optics].
  - [10] B. Han, J. M. Fitzgerald, L. Lackner, R. Rosati, M. Eschmann, F. Eilenberger, T. Taniguchi, K. Watanabe, M. Symperek, E. Malic, and C. Schneider, *Phys. Rev. Lett.* **134**, 076902 (2025).
  - [11] F. Peyskens, C. Chakraborty, M. Muneeb, D. Van Thourhout, and D. Englund, *Nat. Commun.* **10**, 4435 (2019).
  - [12] C. Errando-Herranz, E. Schöll, R. Picard, M. Laini, S. Gyger, A. W. Elshaari, A. Branny, U. Wennberg, S. Barbat, T. Renaud, M. Sartison, M. Brotons-Gisbert, C. Bonato, B. D. Gerardot, V. Zwiller, and K. D. Jöns, *ACS Photonics* **8**, 1069 (2021).
  - [13] A. R.-P. Montblanch, M. Barbone, I. Aharonovich, M. Atatüre, and A. C. Ferrari, *Nat. Nanotechnol.* **18**, 555 (2023).
  - [14] P. Tonndorf, R. Schmidt, R. Schneider, J. Kern, M. Buscema, G. A. Steele, A. Castellanos-Gomez, H. S. J. van der Zant, S. Michaelis de Vasconcellos, and R. Bratschkitsch, *Optica* **2**, 347 (2015).
  - [15] S. Kumar, A. Kaczmarczyk, and B. D. Gerardot, *Nano Lett.* **15**, 7567 (2015).
  - [16] C. Palacios-Berraquero, D. M. Kara, A. R.-P. Montblanch, M. Barbone, P. Latawiec, D. Yoon, A. K. Ott, M. Loncar, A. C. Ferrari, and M. Atatüre, *Nat. Commun.* **8**, 15093 (2017).
  - [17] A. Branny, S. Kumar, R. Proux, and B. D. Gerardot, *Nat. Commun.* **8**, 15053 (2017).
  - [18] L. N. Tripathi, O. Iff, S. Betzold, L. Dusanowski, M. Emmerling, K. Moon, Y. J. Lee, S.-H. Kwon, S. Höfling, and C. Schneider, *ACS Photonics* **5**, 1919 (2018).
  - [19] M. R. Rosenberger, C. K. Dass, H.-J. Chuang, S. V. Sivaram, K. M. McCreary, J. R. Hendrickson, and B. T. Jonker, *ACS Nano* **13**, 904 (2019).
  - [20] C. Chakraborty, N. R. Jungwirth, G. D. Fuchs, and A. N. Vamivakas, *Phys. Rev. B* **99**, 045308 (2019).
  - [21] K. Parto, S. I. Azzam, K. Banerjee, and G. Moody, *Nat. Commun.* **12**, 3585 (2021).

- [22] C. E. Stevens, H.-J. Chuang, M. R. Rosenberger, K. M. McCreary, C. K. Dass, B. T. Jonker, and J. R. Hendrickson, *ACS Nano* **16**, 20956 (2022).
- [23] A. M. Kumar, D. Yagodkin, R. Rosati, D. J. Bock, C. Schattauer, S. Tobisch, J. Hagel, B. Höfer, J. N. Kirchhof, P. Hernández López, K. Burfeindt, S. Heeg, C. Gahl, F. Libisch, E. Malic, and K. I. Bolotin, *Nat. Commun.* **15**, 7546 (2024).
- [24] F. C. M. Wu, S.-H. Wu, B. Fang, X. Li, J. Zheng, J. A. C. Incorvia, and E. T. Yu, *Nano Lett.* **25**, 10983 (2025).
- [25] L. Linhart, M. Paur, V. Smejkal, J. Burgdörfer, T. Mueller, and F. Libisch, *Phys. Rev. Lett.* **123**, 146401 (2019).
- [26] Y.-M. He, G. Clark, J. R. Schaibley, Y. He, M.-C. Chen, Y.-J. Wei, X. Ding, Q. Zhang, W. Yao, X. Xu, C.-Y. Lu, and J.-W. Pan, *Nat. Nanotechnol.* **10**, 497 (2015).
- [27] A. Srivastava, M. Sidler, A. V. Allain, D. S. Lembke, A. Kis, and A. Imamoglu, *Nat. Nanotechnol.* **10**, 491 (2015).
- [28] M. Koperski, K. Nogajewski, A. Arora, V. Cherkez, P. Mallet, J.-Y. Veuillen, J. Marcus, P. Kossacki, and M. Potemski, *Nat. Nanotechnol.* **10**, 503 (2015).
- [29] G. D. Shepard, O. A. Ajayi, X. Li, X.-Y. Zhu, J. Hone, and S. Strauf, *2D Mater.* **4**, 021019 (2017).
- [30] Y. Luo, G. D. Shepard, J. V. Ardelean, D. A. Rhodes, B. Kim, K. Barmak, J. C. Hone, and S. Strauf, *Nat. Nanotechnol.* **13**, 1137 (2018).
- [31] Q. Wang, J. Maisch, F. Tang, D. Zhao, S. Yang, R. Joos, S. L. Portalupi, P. Michler, and J. H. Smet, *Nano Lett.* **21**, 7175 (2021).
- [32] L. Sortino, P. G. Zotev, C. L. Phillips, A. J. Brash, J. Cambiasso, E. Marensi, A. M. Fox, S. A. Maier, R. Sapienza, and A. I. Tartakovskii, *Nat. Commun.* **12**, 6063 (2021).
- [33] J.-C. Drawer, V. N. Mitryakhin, H. Shan, S. Stephan, M. Gittinger, L. Lackner, B. Han, G. Leibeling, F. Eilenberger, R. Banerjee, S. Tongay, K. Watanabe, T. Taniguchi, C. Lienau, M. Silies, C. Anton-Solanas, M. Esmann, and C. Schneider, *Nano Lett.* **23**, 8683 (2023).
- [34] A. Paralikis, C. Piccinini, A. A. Madigawa, P. Metuh, L. Vannucci, N. Gregersen, and B. Munkhbat, *npj 2D Mater. Appl.* **8**, 59 (2024).
- [35] S. Kumar, M. Brotóns-Gisbert, R. Al-Khuzheyri, A. Branny, G. Ballesteros-Garcia, J. F. Sánchez-Royo, and B. D. Gerardot, *Optica* **3**, 882 (2016).
- [36] R. S. Daveau, T. Vandekerckhove, A. Mukherjee, Z. Wang, J. Shan, K. F. Mak, A. N. Vamivakas, and G. D. Fuchs, *APL Photonics* **5**, 096105 (2020).
- [37] M. von Helversen, L. Greten, I. Limame, C.-W. Shih, P. Schlaugat, C. Antón-Solanas, C. Schneider, B. Rosa, A. Knorr, and S. Reitzenstein, *2D Mater.* **10**, 045034 (2023).
- [38] C. Piccinini, A. Paralikis, J. F. Neto, A. A. Madigawa, P. Wyborski, V. Remesh, L. Vannucci, N. Gregersen, and B. Munkhbat, *Commun. Phys.* **8**, 158 (2025).
- [39] H. Kim, J. S. Moon, G. Noh, J. Lee, and J.-H. Kim, *Nano Lett.* **19**, 7534 (2019).
- [40] E. J. Lenferink, T. LaMountain, T. K. Stanev, E. Garvey, K. Watanabe, T. Taniguchi, and N. P. Stern, *ACS Photonics* **9**, 3067 (2022).
- [41] A. Paralikis, P. Wyborski, P. Metuh, N. Gregersen, and B. Munkhbat, *Tunable and low-noise wse<sub>2</sub> quantum emitters for quantum photonics* (2025), arXiv:2507.03355 [physics.optics].
- [42] H. Zhao, M. T. Pettes, Y. Zheng, and H. Htoon, *Nat. Commun.* **12**, 6753 (2021).
- [43] L. C. Flatten, L. Weng, A. Branny, S. Johnson, P. R. Dolan, A. A. P. Trichet, B. D. Gerardot, and J. M. Smith, *Appl. Phys. Lett.* **112**, 191105 (2018).
- [44] C. Robert, R. Picard, D. Lagarde, G. Wang, J. Echeverry, F. Cadiz, P. Renucci, A. Högele, T. Amand, X. Marie, *et al.*, *Phys. Rev. B* **94**, 155425 (2016).
- [45] G. Moody, J. Schaibley, and X. Xu, *J. Opt. Soc. Am. B* **33**, C39 (2016).
- [46] L. Yu, M. Deng, J. L. Zhang, S. Borghardt, B. Kardynal, J. Vučković, and T. F. Heinz, *Nano Lett.* **21**, 2376 (2021).
- [47] R. Brouri, A. Beveratos, J.-P. Poizat, and P. Grangier, *Opt. Lett.* **25**, 1294 (2000).
- [48] J. Klein, M. Lorke, M. Florian, F. Sigger, L. Sigl, S. Rey, J. Wierzbowski, J. Cerne, K. Müller, E. Mitterreiter, *et al.*, *Nat. Commun.* **10**, 2755 (2019).
- [49] Y.-M. He, O. Iff, N. Lundt, V. Baumann, M. Davanco, K. Srinivasan, S. Höfling, and C. Schneider, *Nat. Commun.* **7**, 13409 (2016).
- [50] O. Iff, Y.-M. He, N. Lundt, S. Stoll, V. Baumann, S. Höfling, and C. Schneider, *Optica* **4**, 669 (2017).
- [51] J. Kutrowska-Girzycka, E. Zieba-Ostójska, D. Biegańska, M. Florian, A. Steinhoff, E. Rogowicz, P. Mrowiński, K. Watanabe, T. Taniguchi, C. Gies, S. Tongay, C. Schneider, and M. Syperek, *Appl. Phys. Rev.* **9**, 041410 (2022).
- [52] C. Androulidakis, K. Zhang, M. Robertson, and S. Tawfik, *2D Mater.* **5**, 032005 (2018).
- [53] A. A. Madigawa, M. A. Jacobsen, C. Piccinini, P. Wyborski, A. Garcia Jr., S. F. C. da Silva, A. Rastelli, B. Munkhbat, and N. Gregersen, *Adv. Quantum Technol.*, e2500128 (2025).
- [54] D. A. Vajner, P. Holewa, E. Zieba-Ostójska, M. Wasiluk, M. von Helversen, A. Sakanas, A. Huck, K. Yvind, N. Gregersen, A. Musiał, M. Syperek, E. Semenova, and T. Heindel, *ACS Photonics* **11**, 339 (2024).
- [55] J. P. Echeverry, B. Urbaszek, T. Amand, X. Marie, and I. C. Gerber, *Phys. Rev. B* **93**, 121107 (2016).
- [56] L. Vannucci, J. F. Neto, C. Piccinini, A. Paralikis, N. Gregersen, and B. Munkhbat, *Phys. Rev. B* **109**, 245304 (2024).
- [57] A. Steinhoff, S. Wilksen, I. Solovev, C. Schneider, and C. Gies, *Phys. Rev. B* **111**, 195431 (2025).
- [58] O. Iff, Q. Buchinger, M. Moczala-Dusanowska, M. Kamp, S. Betzold, M. Davanco, K. Srinivasan, S. Tongay, C. Antón-Solanas, S. Höfling, and C. Schneider, *Nano Lett.* **21**, 4715 (2021).
- [59] T. Cai, J.-H. Kim, Z. Yang, S. Dutta, S. Aghaeimeibodi, and E. Waks, *ACS Photonics* **5**, 3466 (2018).
- [60] A. Castellanos-Gomez, M. Buscema, R. Molenaar, V. Singh, L. Janssen, H. S. J. van der Zant, and G. A. Steele, *2D Mater.* **1**, 011002 (2014).
- [61] P. Wyborski, A. Tuktamyshev, M. A. Jacobsen, A. A. Madigawa, S. Vichi, N. Gregersen, S. Sanguinetti, and B. Munkhbat, *Adv. Quantum Technol.*, e2500159 (2025).